

**Cite this article as:** Geng Yongxiang, Zheng Haizhong, Li Guifa, et al. Electrochemical Corrosion Behavior of Ni-based Single-Crystal Superalloy Treated by Laser Shock Peening[J]. Rare Metal Materials and Engineering, 2023, 52(08): 2721-2731.

ARTICLE

# Electrochemical Corrosion Behavior of Ni-based Single-Crystal Superalloy Treated by Laser Shock Peening

Geng Yongxiang<sup>1,2</sup>, Zheng Haizhong<sup>1,2</sup>, Li Guifa<sup>1,2</sup>, Xiao Yixin<sup>1,2</sup>

<sup>1</sup> National Defense Key Disciplines Laboratory of Light Alloy Processing Science and Technology, Nanchang Hangkong University, Nanchang 330063, China; <sup>2</sup> School of Materials Science and Engineering, Nanchang Hangkong University, Nanchang 330063, China

**Abstract:** Ni-based single-crystal (SC) superalloys were treated by laser shock peening (LSP) and then exposed at 750 and 850 °C for 2 h. The electrochemical corrosion behavior of the as-obtained specimens was investigated in 3.5wt% NaCl solution. The results show an increase in the corrosion resistance of SC alloy treated by LSP; it is related to the compressive residual stresses (CRS) and significantly different dislocation structures in  $\gamma/\gamma'$  phases. The non-uniformly distributed dislocations in  $\gamma/\gamma'$  phases raise the two-phase misfit. The electrochemical corrosion tests of LSP-treated specimens after heat exposure indicate that CRS and two-phase misfit are the two major factors influencing the corrosion resistance of SC alloys. CRS can enhance the corrosion resistance while the two-phase misfit deteriorates the corrosion resistance of SC alloys. In addition, the improved corrosion resistance of SC superalloys is linked to the formation of Ta<sub>2</sub>O<sub>5</sub> and WO<sub>3</sub> oxides.

**Key words:** Ni-based SC superalloy; laser shock peening; electrochemical corrosion; lattice misfit; CRS

The excellent physical and mechanical properties of Ni-based SC superalloys including creep, fatigue, and corrosion resistance, make them widely used as turbine blade materials in aircraft engines and industrial gas engines<sup>[1]</sup>. For offshore areas, aircraft are generally parked on ships or coastal airports, making their parts unavoidably exposed to moist salt-containing environments. Some adverse impacts, such as pitting corrosion on superalloy surfaces, increase the potential risk of failure of superalloy parts. Therefore, corrosion failure has become a major focus for the manufacture and evaluation of superalloy parts, especially in service environments with high humidity and high NaCl concentration<sup>[2]</sup>. Thus, the interest on the electrochemical corrosion of Ni-based SC superalloys in NaCl-containing aqueous solution at room temperature has dramatically risen<sup>[3-4]</sup>.

In recent years, peening methods, such as shot peening (SP)<sup>[5]</sup>, hammer peening (HP)<sup>[6]</sup>, and LSP<sup>[7]</sup>, have been used to improve the corrosion resistance of metallic materials. Among these methods, LSP is effective in enhancing the corrosion resistance of metallic materials by generating a large number

of crystal defects, high-level CRS, and deep grain refinement layers on material surfaces. LSP can improve the corrosion resistance of various polycrystalline metallic materials and alloys, such as steels<sup>[8]</sup>, aluminum alloys<sup>[9]</sup>, and superalloys<sup>[10]</sup>.

Unlike polycrystalline alloys, SC alloys display obvious differences after being processed by SP or LSP methods. First, the plastic deformation modes in different orientations become significantly different due to the inherent anisotropy of SC alloys. Second, the formation and mobility of crystal defects are significantly affected by the coherent interface of phases in alloys<sup>[11]</sup>. Despite this, the influences of the LSP or SP on SC materials and alloys have been explored. Liu et al<sup>[12]</sup> investigated the morphological and crystallographic properties of a robotic hammer peened (RHP) Ni-based SC superalloy and found that surface roughness generated by RHP depends not only on the RHP parameters but also on the initial roughness. Also, the distribution of the RHP-induced crystal reorientation is strongly correlated with the geographically necessary dislocations. Wang et al<sup>[13]</sup> studied the effects of SP on the notched fatigue properties of SC superalloys at elevated

Received date: November 27, 2022

Foundation item: Youth Science Fund Project of Jiangxi Province (20212BAB214037); National Natural Science Foundation of China (52271057, 52071172, 51361026); Open Foundation of National Defense Key Disciplines Laboratory of Light Alloy Processing Science and Technology (EG202101419); PhD Research Startup Foundation of Nanchang Hangkong University (EA202001199)

Corresponding author: Zheng Haizhong, Ph.D., Professor, School of Materials Science and Engineering, Nanchang Hangkong University, Nanchang 330063, P. R. China, Tel: 0086-791-86453203, E-mail: zhzh@nchu.edu.cn

Copyright © 2023, Northwest Institute for Nonferrous Metal Research. Published by Science Press. All rights reserved.

temperatures and noticed that the beneficial effect provided by SP reaches above 14.8% against the as-machined specimen due to factors like the high-density tangled dislocations, cold hardening, and disorientation. Kubásek et al.<sup>[14]</sup> investigated the effect of LSP on the microstructure and defect structure of monocrystalline copper. The LSP-induced dislocations are homogeneously distributed on the cross-section of Cu single crystal along the single slip plane, and density gradually decreases in the direction of the specimen center. Lu et al.<sup>[15]</sup> treated Ni-based SC superalloys by LSP and found that LSP induces inhomogeneous deformation to  $\gamma'$  precipitates and  $\gamma$  channels, resulting in a significant hardening effect. Our research group also reported the effects of LSP on Ni-based SC superalloys<sup>[16-18]</sup>. However, despite the efforts, satisfactory research focusing on the LSP of single crystals is lacking. It is still unclear whether LSP can be used to improve the electrochemical corrosion resistance of SC alloys at room temperature, as well as how high-temperature heat exposure affects the electrochemical corrosion behavior of LSP-treated SC alloys.

Therefore, the electrochemical corrosion behavior of LSP-treated Ni-based SC superalloys with and without heat exposure was investigated in 3.5wt% NaCl solution at room temperature. In the end, the residual stresses, microhardness, and typical microstructural features were firstly characterized on the surface layers of LSP-treated specimens. Secondly, the effects of LSP on the open circuit potential (OCP) potentiodynamic polarization (PD), electrochemical impedance spectra (EIS), corrosion morphologies, and corrosion products of LSP-treated specimens with and without heat exposure were explored. Finally, the influences of LSP on the electrochemical corrosion behavior of SC alloys and the changes in the electrochemical corrosion behavior of LSP-treated SC alloys after heat exposure were evaluated.

## 1 Experiment

Ni-based SC superalloys with [001] orientation (dimensions 10 mm×10 mm×3 mm in length×width×thickness) were used in the study. The microstructure of SC superalloy consisted of a dual phase microstructure with an ordered  $L1_2$  structured  $\gamma'$  phase and a face-centered cubic (fcc) structured  $\gamma$  phase. The chemical composition (wt%) was determined as 6.90Ta, 8.21W, 4.25Cr, 5.80Al, 8.95Co, 2.06Mo, 2.24Re, 0.70Nb, 0.11Hf, 0.023C, and balanced Ni. The processing method and parameter selection basis of LSP can be found in Ref. [18]. Only one side of specimen surfaces (10 mm×10 mm) with [001] orientation was treated by LSP. To investigate the effects of heat exposure on the corrosion resistance of LSP-treated SC alloys, these samples were successively exposed at 750 and 850 °C for 2 h under a vacuum environment ( $5 \times 10^{-3}$  Pa) followed by cooling to room temperature. The SC alloy maintained a stable microstructure without other precipitates during short-term heat exposure at medium and low temperatures. For simplicity purposes, the LSP-treated specimens were named as LSP, while the untreated specimens were called as Non-LSP.

The electrochemical corrosion tests were carried out in 3.5wt% NaCl solution at room temperature using a standard three-electrode system connected to a CHI 660E workstation. Saturated calomel, platinum foil, and the specimens (immersed area 1 cm<sup>2</sup>) were used as reference electrode, counter electrode, and working electrode, respectively. Unexposed surfaces of the testing specimens were covered by epoxy resin and a wire was connected to the opposite surface of the test surface. The experiments were conducted in the following sequence. (1) OCP tests for 4000 s; (2) EIS tests using a 10 mV RMS sinusoidal signal at frequencies of 100 kHz to 0.1 Hz; (3) PD tests at potentials from -1 V to 1 V at a scanning rate of 1 mV/s. According to a previous report<sup>[8]</sup>, EIS data were fitted using a relevant equivalent circuit through Z Fit software. Corrosion current density ( $i_{\text{corr}}$ ) and corrosion potential ( $E_{\text{corr}}$ ) were determined from the polarization curves using the Tafel extrapolation method.

The X-ray diffraction (XRD) patterns were measured by a Bruker D8ADVANCE diffractometer equipped with a Cu K $\alpha$  radiation source (X-ray wavelength=0.154 178 nm) at a scanning speed of 1.2°/min. An MVS-1000JMT2 microhardness tester with a load of 200 g and holding time of 10 s was used for the measurement of Vickers microhardness. The XRD patterns and microhardness along the specimen depth were evaluated by removing the specimens layer by layer via electrolytic polishing with 12.5vol% sulfuric acid and 87.5vol% methanol. Optical microscopy (OM, ZEISS SMARTPROOF-5), scanning electron microscopy (SEM, HITACHISU3500) equipped with energy dispersive spectroscopy (EDS, Oxford), and transmission electron microscopy (TEM, JEOL JEM-2100F) were employed for surface microstructure and morphology observations. The chemical compositions of corrosion products were identified by X-ray photoelectron spectroscopy (XPS, Thermo Fisher ESCALAB Xi+). The standard carbon C 1s peak at 284.6 eV was adopted for calibration of binding energy, and Avantage 5.52 software was used for XPS data processing.

## 2 Results and Discussion

### 2.1 Phase, residual stress, and microhardness analysis

The phase transformation, residual stress, and microhardness distribution of the specimens are shown in Fig.1 and Fig. 2. Obviously, no phase transformation occurs after LSP, and each diffraction peak consists of overlapped peaks associated with the  $\gamma$  and  $\gamma'$  phases (Fig. 1a). The diffraction peaks of LSP-treated specimen shift toward lower angles with respect to their original positions (Fig. 1b and 1c), indicating the formation of compressive residual stresses<sup>[2]</sup>. After heat exposure at 750 and 850 °C for 2 h, the LSP-treated specimens exhibit a single peak (Fig. 1d), suggesting precipitation of no new phases.

As shown in Fig.2a, a maximal CRS with a value of about -250 MPa is observed on the surface. As depth rises, the residual stress decreases gradually until zero at about 600  $\mu\text{m}$  in depth. Since CRS induced by LSP can be attributed to the formation of dislocations and other defects<sup>[19]</sup>, LSP may have

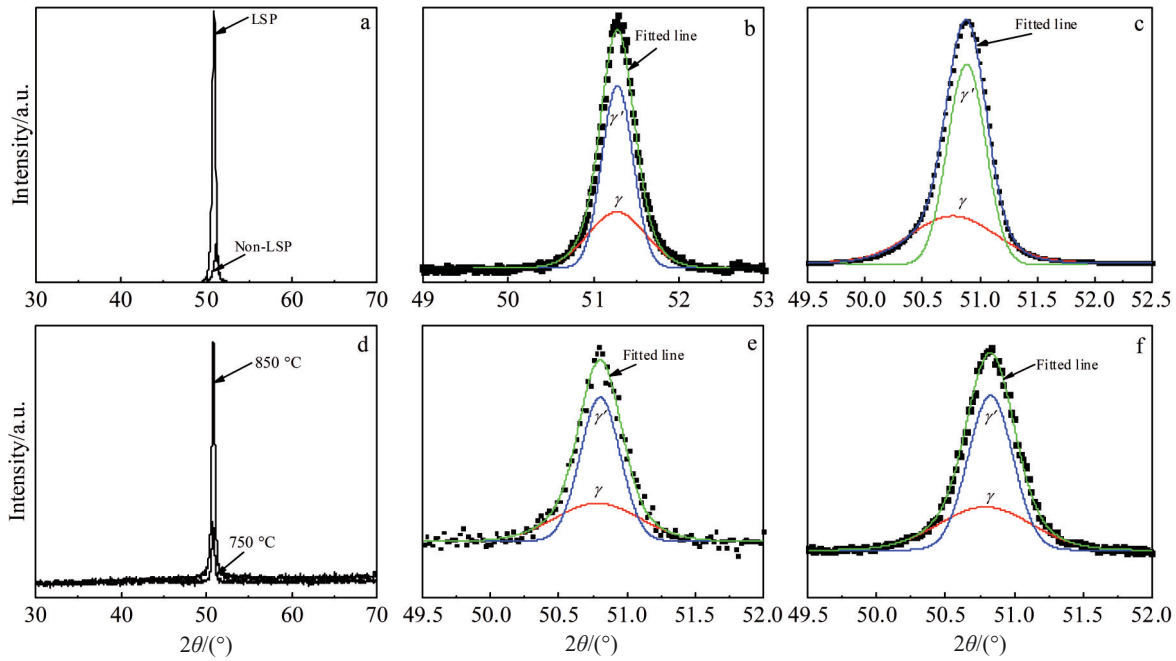


Fig.1 XRD patterns (a) and corresponding separated diffraction peaks of untreated (b) and LSP-treated (c) specimens without heat exposure; XRD patterns (d) and corresponding separated diffraction peaks of LSP-treated specimens after heat exposure at 750 °C (e) and 850 °C (f) for 2 h

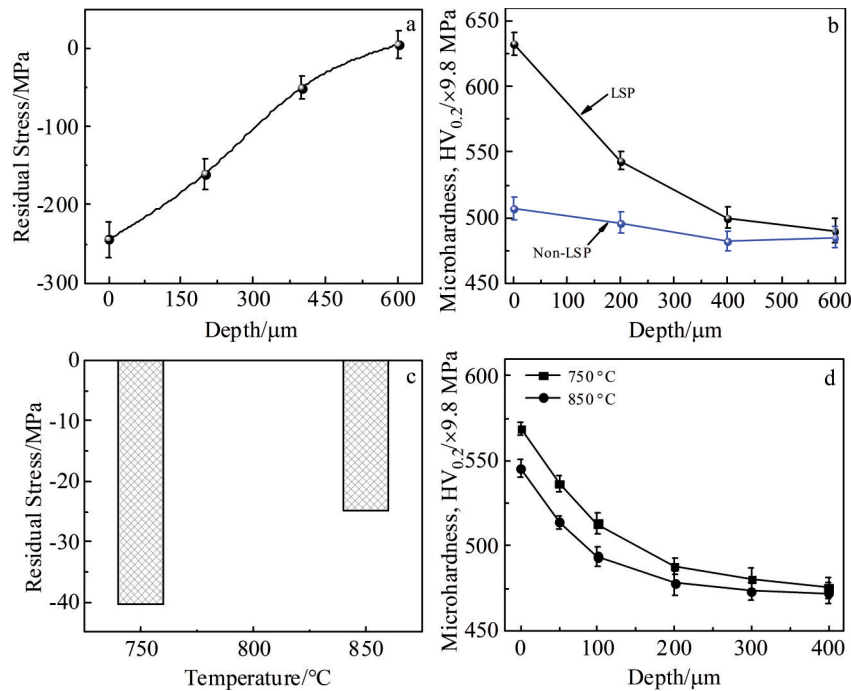


Fig.2 Residual stresses (a, c) and microhardness values along the depth direction (b, d) of LSP-treated specimens: (a, b) without heat exposure and (c, d) heat exposure at 750 and 850 °C for 2 h

also changed the microstructures of materials. The microhardness in the depth direction of the LSP-treated specimen exhibits an identical pattern as CRS (Fig.2b). The enhanced microhardness can be attributed to the work hardening of the material surface caused by LSP. Similarly, the CRS becomes almost completely relaxed (Fig.2c) and the

microhardness is reduced (Fig.2d) after heat exposure at 750 and 850 °C for 2 h. The lattice misfit  $\delta$  of the two phases can be defined as  $\delta=2(\alpha_{\gamma}-\alpha_{\alpha})/(\alpha_{\gamma}+\alpha_{\alpha})$ <sup>[20]</sup>, and calculated from the lattice parameters determined from the separated peaks (Table 1). The lattice misfit represents the stability and stress state of the two-phase interface. For alloys with lattice misfits of

**Table 1** Diffraction angle, full width at half maximum, lattice parameters and misfit of the  $\gamma/\gamma'$  two phases obtained from their separated diffraction peaks

Treatment	$2\theta_{(001)}/(^{\circ})$		$\beta_{(001)\gamma}/(^{\circ})$		$a/\text{nm}$		$\delta$
	$\gamma$	$\gamma'$	$\gamma$	$\gamma'$	$\gamma$	$\gamma'$	
Non-LSP, 25 °C	51.075	51.082	0.67691	0.36432	0.357802	0.357741	-0.013
LSP, 25 °C	50.767	50.885	0.87363	0.39097	0.358314	0.357549	-0.216
LSP, 750 °C	50.788	50.828	0.6730	0.3272	0.359248	0.358983	-0.073
LSP, 850 °C	50.782	50.804	0.6276	0.2946	0.359287	0.359140	-0.041

lower absolute value, the coherent strain of  $\gamma/\gamma'$  interface is smaller. Therefore, LSP increases the coherent strain of the  $\gamma/\gamma'$  interface by inducing plastic deformation. Inversely, the lattice misfits of the two phases of LSP-treated specimens significantly decrease after heat exposure at 750 and 850 °C for 2 h.

## 2.2 Microstructure and surface morphology

Near-surface TEM observations of untreated and LSP-treated specimens without heat exposure are presented in Fig. 3a–3d. The  $\gamma'$  phases exhibit cubic structures with  $\{100\}$  facets, and also form coherent interfaces with continuous  $\gamma$  phase in narrow parallel  $\gamma$  channels between the  $\gamma'$  cuboids (Fig. 3a). Such inherent  $\gamma/\gamma'$  two-phase structures challenge dislocations to cut into the rigid  $\gamma'$  phase, thereby limiting the movement of dislocation in  $\gamma$  channels<sup>[21]</sup>. In Fig. 3b–3d, different dislocation distributions are noticed in  $\gamma/\gamma'$  two phases. High-density dislocations are mainly distributed in  $\gamma$  channels to further form dislocation pileups due to the complex dislocation interactions. Several dislocations are also observed in  $\gamma'$  phases, first originating from  $\gamma$  phase and then shearing into  $\gamma'$  phases via overcoming the coherent

strengthening effect of  $\gamma/\gamma'$  interface. In general, dislocations in the  $\gamma$  phase are propagated into the  $\gamma'$  phase as dislocation pairs, resulting in the formation of anti-phase boundaries and stacking faults<sup>[22]</sup>. As a result, stacking faults are observed in  $\gamma'$  phases. After heat exposure at 750 and 850 °C for 2 h (Fig. 3e and 3f), dislocation densities in  $\gamma$  and  $\gamma'$  phases are reduced due to the annihilation and rearrangement of dislocations during heat exposure.

The density of dislocations ( $\rho_{hkl}$ ) in  $\gamma/\gamma'$  two phases can be predicted according to Eq.(1)<sup>[23]</sup>:

$$\rho_{hkl} = \frac{\sqrt{3}}{2b} \frac{\beta_{hkl}^2 \cos \theta_{hkl}}{k\lambda \tan \theta_{hkl}} \quad (1)$$

where  $b$  represents the magnitude of the Burgers vector,  $K$  is the Scherer's factor of 0.9,  $\lambda$  refers to the wavelength of the X-ray, and  $\beta_{hkl}$  and  $\theta_{hkl}$  are the full widths at half maximum of diffraction peak and diffraction angle in  $(hkl)$  crystal plane, respectively.

The diffraction angle ( $2\theta_{001}$ ) and full width at half maximum ( $\beta_{001}$ ) of  $\gamma/\gamma'$  two phases in (001) crystal plane are obtained from their separated diffraction peaks (Table 1). In Ni-based SC superalloy, Burger's vector of a full dislocation for  $\gamma'$  phase

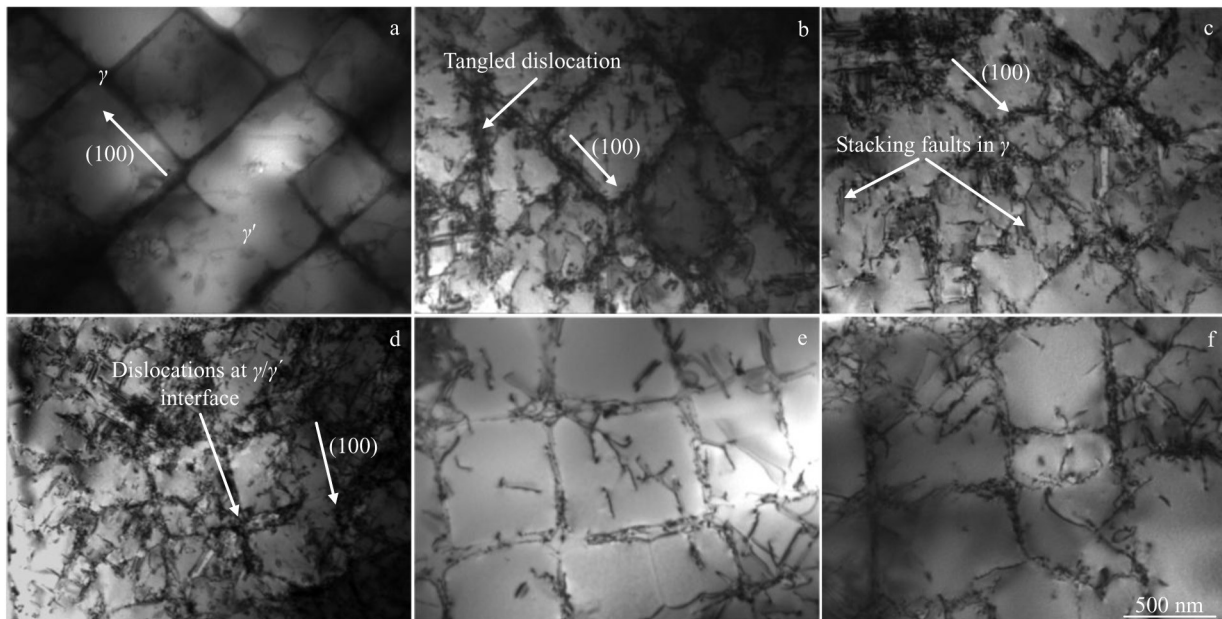


**Fig.3** Near-surface TEM images of untreated (a) and LSP-treated specimens without heat exposure (b–d) and with heat exposure at 750 °C (e) and 850 °C (f) for 2 h

with an  $L1_2$  structure can be written as  $b=a\langle 110 \rangle$  (where  $a$  is lattice parameter), representing twice in the magnitude of  $\gamma$  phase with an fcc structure<sup>[24]</sup>. Therefore, the dislocation density in  $\gamma/\gamma'$  two phases is calculated by Eq.(1), confirming the distribution of high-density dislocations induced by LSP in  $\gamma$  phase (Fig.4). Also, heat exposure decreases the dislocation density in  $\gamma$  and  $\gamma'$  phase, which further reduces the CRS and two-phase misfit.

The surface morphologies and surface roughness of untreated and LSP-treated specimens without heat exposure are provided in Fig. 5. LSP results in significantly increased average surface roughness ( $R_a$ ), attributed to the dimples generated by LSP. Since the water is employed as a confinement layer during LSP, it may cause the laser bending and self-focus, leading to the non-uniform distribution of dimples<sup>[25]</sup>. In addition, surface roughness as a parameter of technical surface plays an important role in determining the performance of industrial factors like corrosion, wear, and fatigue. High surface roughness increases the effective contact area between the material surface and the corrosive medium,

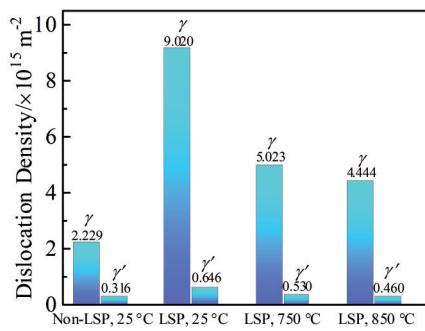


Fig.4 Dislocation densities in  $\gamma/\gamma'$  two phases of the untreated and LSP-treated specimens with and without heat exposure

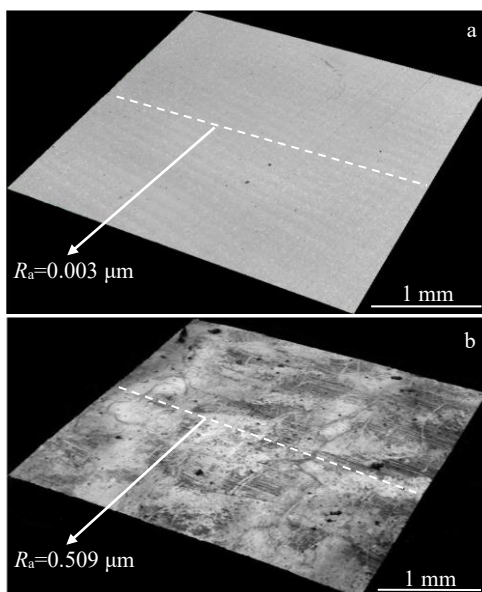


Fig.5 Surface morphologies and surface roughness of the untreated (a) and LSP-treated (b) specimens without heat exposure

thereby deteriorating the corrosion behavior<sup>[26]</sup>.

## 2.3 Electrochemical evaluation

### 2.3.1 Corrosion tests

The OCP of the untreated and LSP-treated specimens with and without heat exposure as a function of time is displayed in Fig. 6. Initially, the OCP of the untreated and LSP-treated specimens without heat exposure shifts to more negative magnitudes with the increase in time. The high OCP for the untreated and LSP-treated specimens without heat exposure at the start of testing is resulted from the air-formed protective film formation. The OCP of the LSP-treated specimen shifts toward the positive direction compared to the untreated specimen. In general, the positive shift in OCP will indicate the formation of a passive film, and conversely, the negative shift will be related to local breakdown or dissolution of the film or no film formation<sup>[27]</sup>. Therefore, more positive OCP indicates an increase in corrosion resistance. After heat exposure, the OCP of the LSP-treated specimens shows a significant shift toward the negative direction. However, compared with heat exposure at 750 °C, OCP exhibits a slightly positive shift after heat exposure at 850 °C, indicating a possible increase in corrosion resistance.

The PD curves of untreated and LSP-treated specimens with and without heat exposure are given in Fig.7. Corrosion potential ( $E_{\text{corr}}$ ), corrosion current density ( $i_{\text{corr}}$ ) and passivation potential ( $\Delta E_p$ ) are obtained through the fitting of the curves by the Tafel extrapolation method. The calculated results are listed in Table 2. LSP-treated specimens without heat exposure have the lowest  $i_{\text{corr}}$  and the broadest  $\Delta E_p$ . After heat exposure,  $i_{\text{corr}}$  increases and  $\Delta E_p$  becomes narrow but it shows low  $i_{\text{corr}}$  and broad  $\Delta E_p$  as the heat exposure temperature increases. In general, lower  $i_{\text{corr}}$  and broader  $\Delta E_p$  will indicate a lower corrosion rate, while more positive  $E_{\text{corr}}$  means higher chemical stability and lower corrosion tendency<sup>[28]</sup>. The LSP-treated specimen without heat exposure exhibits more positive corrosion potential and lower corrosion current density, indicating better corrosion resistance. Similarly, increasing the heat exposure temperature can obtain a relatively high corrosion resistance.

EIS tests were conducted to further explore the electrochemical corrosion behavior of the untreated and LSP-

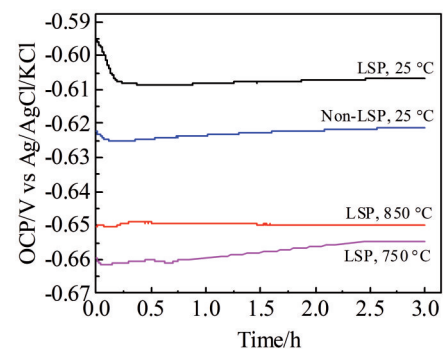


Fig.6 OCP curves of untreated and LSP-treated specimens with and without heat exposure

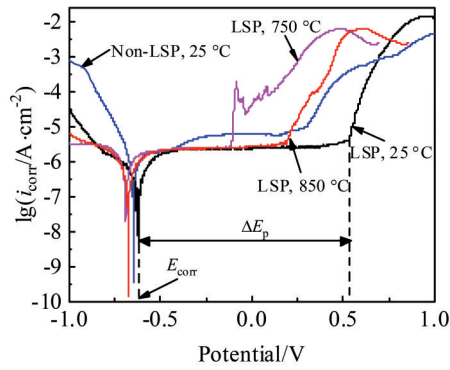


Fig.7 Potentiodynamic polarization curves of untreated and LSP-treated specimens with and without heat exposure

Table 2 Electrochemical parameters obtained from potentiodynamic polarization curves

Specimen	$E_{\text{corr}}/\text{mV}$	$\Delta E_p$	$i_{\text{corr}}/\mu\text{A}\cdot\text{cm}^{-2}$
Non-LSP, 25 °C	-648	0.958	0.7918
LSP, 25 °C	-619	1.141	0.5839
LSP, 750 °C	-693	0.814	3.5960
LSP, 850 °C	-677	0.857	1.0730

treated specimens and the results are gathered in Fig. 8. As shown in Fig. 9, an equivalent circuit model ( $R_s, \text{CPE1}, R_1, \text{CPE2}, R_{\text{ct}}$ ) was used for EIS fitting analysis and the corresponding fitted data are listed in Table 3. Here,  $R_s$  represents the electrolyte resistance,  $R_1$  is the oxide film resistance,  $R_{\text{ct}}$  refers to the charge transfer resistance at the electrolyte-metal interface, CPE represents the constant phase

elements of the oxide film (CPE1) and the double layer (CPE2). CPE is determined by the constant coefficient  $Y$  and diffusion coefficient  $n$ , and  $\chi^2$  denotes fitting error in the scale of  $10^{-4}$  as a reasonable value<sup>[29]</sup>. As shown in Fig. 8a, the Nyquist plot exhibits incomplete capacitive loops. Note that specimens with larger capacitance loops will have lower dissolution rates and higher corrosion resistances<sup>[30]</sup>. The Bode impedance and phase angle plots are given in Fig. 8b and 8c. Note that the modulus value of impedance  $Z$  at the low-frequency range represents the polarization resistance of the material, and the large phase angle in low frequency is attributed to the formation of protective films. The value of  $R_{\text{ct}}$  also reflects the passive film characteristic, and higher  $R_{\text{ct}}$  values imply good resistance<sup>[31]</sup>. Therefore, LSP improves the corrosion resistance of SC superalloys in 3.5wt% NaCl solution when considering the above viewpoints. In Fig. 6–8, the heat exposure decreases the corrosion resistance. However, LSP-treated specimens after heat exposure at 850 °C exhibit higher corrosion resistance than at 750 °C.

### 2.3.2 Corrosion morphologies and corrosion products

The electrochemical corrosion morphologies of untreated and LSP-treated specimens with and without heat exposure are illustrated in Fig. 10. Corrosion deposits are observed on both the untreated and LSP-treated specimen surfaces. However, a large number of corrosion products are deposited on the LSP-treated specimen surface with and without heat exposure when compared to the untreated specimen. This can be related to the higher surface roughness caused by LSP, which accelerates the dissolution of surface materials at the initial corrosion stage. As the corrosion proceeds, the corrosion products are gathered on the specimen surfaces,

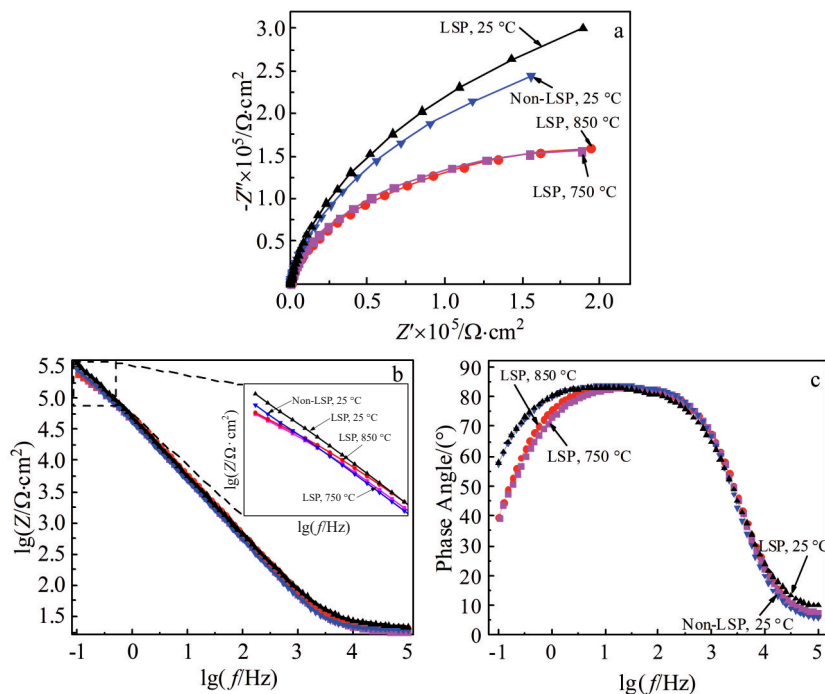


Fig.8 Nyquist plot (a) and Bode plots for impedance (b) and phase angle (c) of untreated and LSP-treated specimens with and without heat exposure

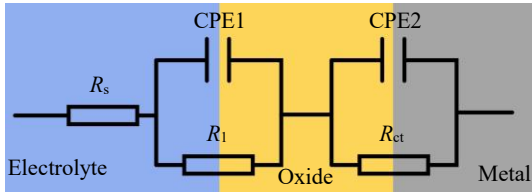


Fig.9 Equivalent circuit model of EIS curves of untreated and LSP-treated specimens with and without heat exposure

serving as a barrier against further corrosion attacks. The existence of helpful compressive residual stresses can also effectively retard the corrosion crack and decrease the corrosion rate, thereby affecting the construction and growth of the passive films as well as improving the corrosion resistance<sup>[9]</sup>. Another factor influencing the corrosion behavior has to do with the dislocation density since dislocations may help the formation of more stable and much thicker passive protection films with improved corrosion resistance<sup>[32]</sup>. Moreover, passive films preferentially grow and instantaneously nucleate at surface defects, such as dislocations and twin boundaries before spreading over to connect, thereby improving the uniformity and compactness of the films<sup>[33]</sup>.

The chemical compositions of corrosion products were explored by EDS point analysis (Table 4) and EDS mapping analysis (Fig. 11). The corrosion products are mainly

composed of O, Ta, and W elements for the untreated and LSP-treated specimens with and without heat exposure. The chemical compositions of corrosion products are further confirmed by XPS (Fig. 12). The survey XPS spectrum contains visible peaks of O, C, W, and Ta elements, while the peak of C element is considered as contamination. Therefore, the oxide scales mainly consist of W and Ta oxides. The high-resolution XPS spectra are displayed in Fig. 12b–12c. The corrosion products mainly include  $Ta_2O_5$  and  $WO_3$ . The low content of other oxides induce unobvious peaks. Therefore, the corrosion resistance of the SC alloy is relevant to the oxides of Ta and W.

#### 2.4 Corrosion behavior

For Ni-based SC superalloys with two-phase microstructure, elements like W, Re, Co, Mo, and Cr will have a typical partition to the  $\gamma$  phase. In contrast, elements like Ni, Al, Ti, and Ta favor the formation of  $\gamma'$  particles<sup>[34]</sup>. As reported in the previous study<sup>[35]</sup>, the pitting resistances of  $\gamma$  and  $\gamma'$  phase can be evaluated by the pitting resistance equivalent number (PREN), defined as  $PREN=1wt\% Cr+3.3wt\% Mo+1.65wt\% W$ . Obviously,  $\gamma'$  phase shows lower pitting resistance than  $\gamma$  phase. Besides, the main forming elements like Ni and Al in  $\gamma'$  phase ( $Ni_3Al$ ) with low standard electrode potentials (Table 5<sup>[36]</sup>) endow  $\gamma'$  phase with good solubility in NaCl solution during corrosion.

The dissolution of  $\gamma'$  phase can thus be considered as the main characteristic of the electrochemical corrosion process.

Table 3 EIS data and equivalent circuit parameters of untreated and LSP-treated specimens with and without heat exposure

Specimen	$R_s/\Omega \cdot cm^2$	CPE <sub>1</sub>		$R_1/\Omega \cdot cm^2$	CPE <sub>2</sub>		$R_{ct}/k\Omega \cdot cm^2$	$\chi^2/\times 10^{-4}$
		$Y_{01}/\times 10^{-15} \Omega^{-1} \cdot cm^2 \cdot s^n$	$n_1$		$Y_{02}/\times 10^{-6} \Omega^{-1} \cdot cm^2 \cdot s^n$	$n_2$		
Non-LSP, 25 °C	6.23	4.958	0.249	21.78	2.094	0.946	339.23	1.10
LSP, 25 °C	7.79	0.2434	0.109	41.37	1.881	0.948	408.09	2.40
LSP, 750 °C	3.55	3.865	0.221	26.86	1.664	0.942	172.68	2.72
LSP, 850 °C	3.81	3.026	0.176	28.41	1.674	0.945	174.81	2.79

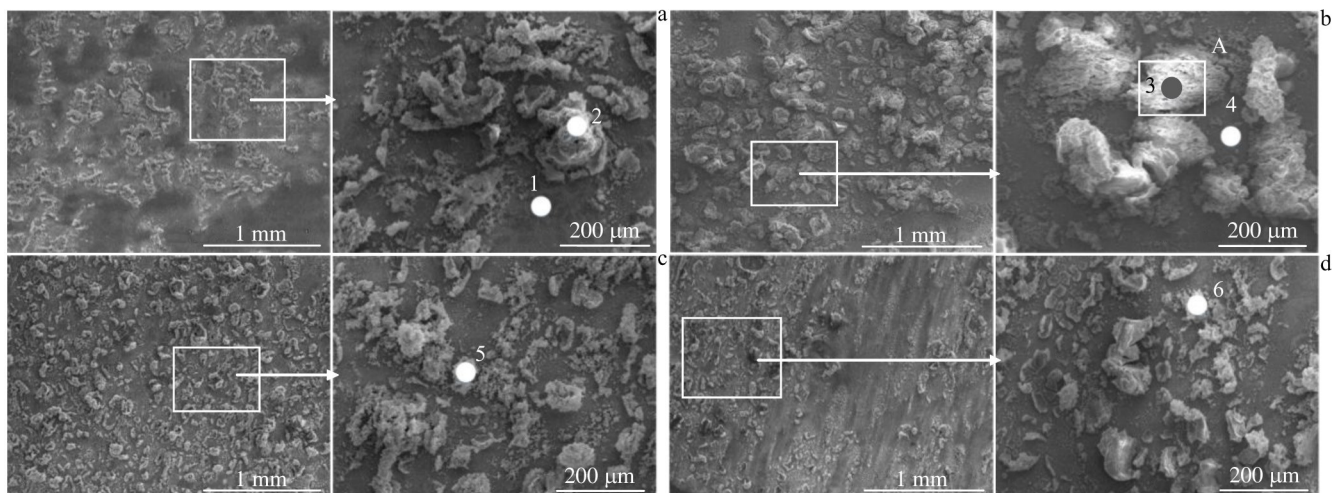
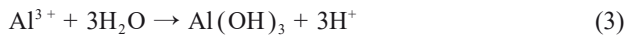
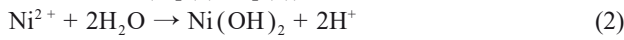


Fig.10 Electrochemical corrosion morphologies of untreated (a) and LSP-treated (b) specimens without heat exposure; LSP-treated specimens after heat exposure at 750 °C (c) and 850 °C (d) for 2 h

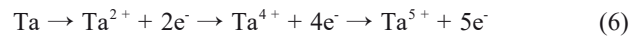
**Table 4** EDS results of the points marked in Fig.10 (at%)

Point	O	Ta	W	Ni	Al	Na
1	-	3.74	3.95	77.33	14.98	-
2	71.89	17.43	7.31	1.54	-	1.83
3	81.74	9.12	6.82	1.33	-	0.90
4	-	4.41	3.76	78.16	13.67	-
5	62.40	22.94	14.67	-	-	-
6	79.85	10.37	6.96	-	-	-

As the main forming elements of  $\gamma'$  phase, Ni and Al dissolved in the solution lead to the destruction of  $\gamma'$  phase structure. Ni and Al cations in the solution are firstly combined with the cathode product of  $\text{OH}^-$  to form hydroxide, and then converted to metal oxides (Eq.(2)–Eq.(5)).



The resulting hydroxides accumulate on the specimen surface, forming a barrier for the substrate against corrosion attack. However,  $\text{Cl}^-$  in solution attacks the hydroxides by forming chloride-containing compounds (such as  $\text{Ni}(\text{OH})\text{Cl}$  or  $\text{NiCl}_2$  and  $\text{Al}(\text{OH})_2\text{Cl}^{2-}$  or  $\text{AlCl}_4^{4-}$ )<sup>[37–38]</sup>, leading to the breakdown of oxide films. Meanwhile, Ta in  $\gamma'$  phase dissolves in the solution due to the destruction of  $\gamma'$  phase structure to finally form insoluble oxide ( $\text{Ta}_2\text{O}_5$ ).  $\text{Ta}_2\text{O}_5$  with high stability is immune to attack by almost all acids except concentrated  $\text{HF}$ <sup>[39]</sup>. Generally,  $\text{Ta}_2\text{O}_5$  forms in a manner by passing through its known intermediate oxidation states of +2 and +4<sup>[40]</sup>.



Similar to the dissolution of  $\gamma'$  phase,  $\gamma$  phase is also dissolved. Since chromium metal can spontaneously form a protective oxide layer of  $\text{Cr}_2\text{O}_3$  in the presence of air ( $\text{Cr} + \text{H}_2\text{O} \rightarrow \text{Cr}_2\text{O}_3 + 6\text{H}^+ + 6\text{e}^-$ ), Cr in  $\gamma$  phase is beneficial to the formation of a protective oxide film on the specimen surface. However, the Cr content should meet the threshold ( $\sim 12\text{wt}\%$  for Fe-Cr and Ni-Cr alloy systems<sup>[41]</sup>) to form intact protective

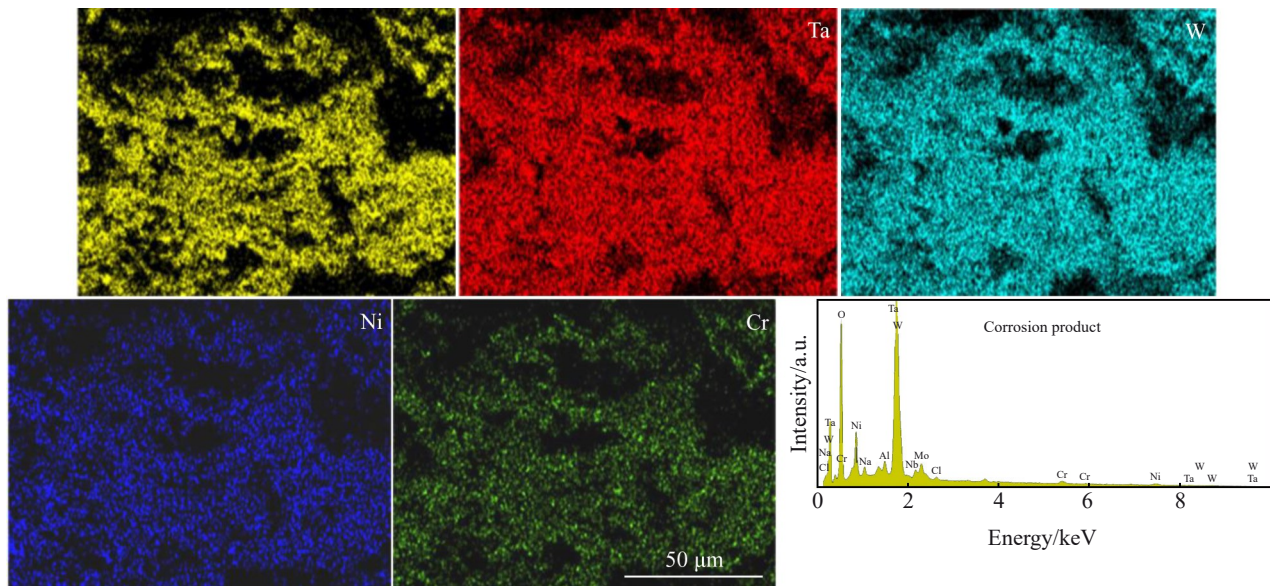


Fig.11 Element mappings of the selected square area A in Fig.10b

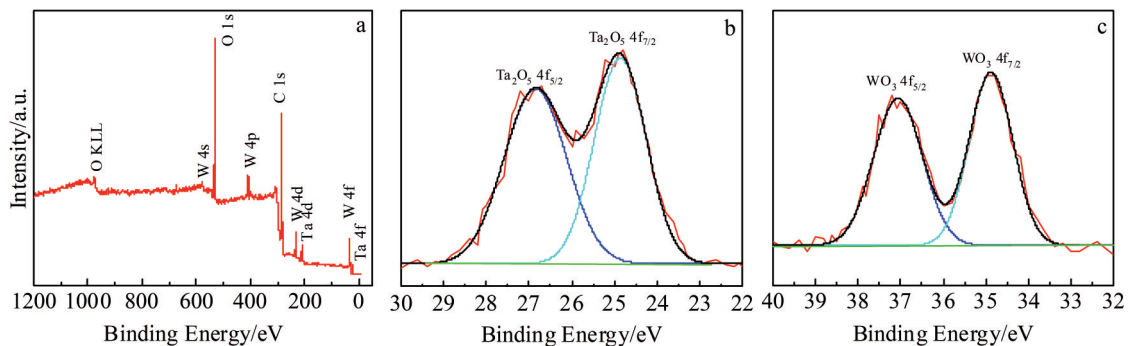
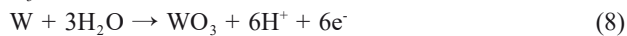


Fig.12 XPS spectra of corrosion products for LSP-treated specimen without heat exposure: (a) survey XPS spectra, (b) high-resolution XPS spectra of Ta, and (c) high-resolution XPS spectra of W

**Table 5** Standard electrode potentials of main elements in investigated SC superalloy<sup>[36]</sup>

Metal	$E^\circ/V$
$\text{Re}^{3+}+3\text{e}^-=\text{Re}$	+0.3
$\text{W}^{3+}+3\text{e}^-=\text{W}$	+0.1
$\text{Mo}^{3+}+3\text{e}^-=\text{Mo}$	-0.20
$\text{Ni}^{2+}+2\text{e}^-=\text{Ni}$	-0.257
$\text{Co}^{2+}+2\text{e}^-=\text{Co}$	-0.28
$\text{Ta}^{3+}+3\text{e}^-=\text{Ta}$	-0.6
$\text{Cr}^{3+}+3\text{e}^-=\text{Cr}$	-0.744
$\text{Nb}^{3+}+3\text{e}^-=\text{Nb}$	-1.099
$\text{Al}^{3+}+3\text{e}^-=\text{Al}$	-1.662

passive films (4.25wt% for the investigated SC alloy). Meanwhile, potentials more positive than 0.8 V (test potential is -1 V to 1 V in this study) can incite chromium (III) oxide to form soluble Cr (VI) species ( $\text{Cr}_2\text{O}_3 + 5\text{H}_2\text{O} \rightarrow 2\text{CrO}_4^{2-} + 10\text{H}^+ + 6\text{e}^-$ )<sup>[41]</sup>. Therefore, Cr provides insufficient protection to form passive films. Moreover, W in  $\gamma$  phase undergoes dissolution to finally form stable oxide ( $\text{WO}_3$ ).  $\text{WO}_3$  is stable at pH values less than 4<sup>[42]</sup>, while other oxides like Co, Mo, Re, Hf, and Nb oxides are not detected by XPS due to their low contents. Therefore, the increased corrosion resistance of SC alloys is related to the formation of protective  $\text{Ta}_2\text{O}_5$  and  $\text{WO}_3$  oxides.



According to the research results, the LSP-treated specimen exhibits better corrosion resistance. Fig. 13 presents the schematic diagram of the corrosion mechanism of LSP-treated specimens in 3.5wt% NaCl solution. As previously reported<sup>[43]</sup>, the CRS and high-density dislocations induced by LSP will result in enhanced corrosion resistance. As shown in Fig. 4, the  $\gamma$  phase possesses high-density dislocations, indicating the existence of higher CRS. CRS effectively

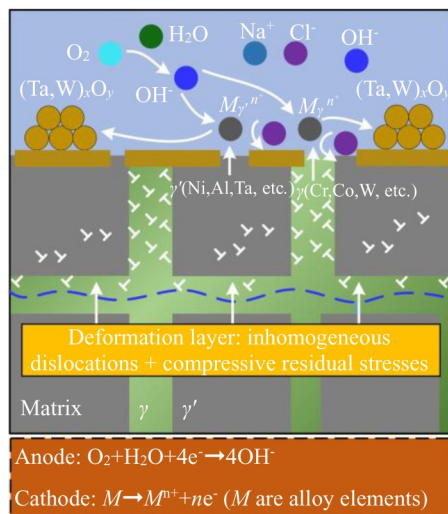


Fig.13 Schematic diagram of corrosion mechanism of LSP-treated specimens in 3.5wt% NaCl solution

restricts the micro-crack propagation and retards stress corrosion cracking initiation in NaCl solution<sup>[44]</sup>. The effect of stress/strain on  $i_{\text{corr}}$  is quantitatively described by Eq.(9)<sup>[45]</sup>.

$$i_{\text{corr}} = i_{\text{corr},0} \left(1 + \frac{\Delta\varepsilon}{\varepsilon_0}\right) \exp\left(\frac{SV_m}{RT}\right) \quad (9)$$

where  $i_{\text{corr},0}$  is the corrosion current density of untreated specimen,  $\Delta\varepsilon$  is the plastic strain,  $\varepsilon_0$  is the strain at the onset of strain hardening,  $S$  is the stress,  $V_m$  is the molar volume of  $7.1 \times 10^{-6} \text{ m}^3 \cdot \text{mol}^{-1}$ ,  $R$  is the standard gas constant, and  $T$  is the temperature. For LSP-treated specimens, compressive residual stresses are introduced in the surface layer, causing the values of  $(1 + \Delta\varepsilon/\varepsilon_0)$  and  $\exp(SV_m/RT)$  to be less than 1. Therefore,  $i_{\text{corr}}$  is reduced, and the corrosion resistance of specimens is enhanced.

High-density dislocations facilitate the diffusion paths for passive elements and simplify the quick formation of protective oxide films<sup>[46]</sup>. However, the dislocation densities in  $\gamma$  and  $\gamma'$  phases look significantly different: high-density dislocations are mainly distributed in the  $\gamma$  phase after LSP. Therefore, elements like Cr, W, Re, Co, Mo, and Cr in the  $\gamma$  phase can rapidly form oxide films due to the existence of high-density dislocations. The induced oxide films slow down the dissolution of  $\gamma'$  phase, thereby enhancing the corrosion resistance of SC alloys.

After heat exposure at 750 and 850 °C for 2 h, the dislocation densities in two phases and two-phase misfit of LSP-treated specimens decrease, while CRS in LSP-treated specimens becomes almost completely relaxed. After heat exposure at 850 °C for 2 h, the LSP-treated specimen exhibits lower dislocation density in both phases with lower two-phase misfit and higher corrosion resistance compared with at 750 °C for 2 h. Therefore, the two-phase misfit influences the corrosion resistance of the LSP-treated specimen. The two-phase misfit can be related to the distribution of dislocation density in two phases. Non-uniformly distributed high-density dislocations in  $\gamma$  and  $\gamma'$  phases will increase the two-phase misfit while a high two-phase misfit will deteriorate the corrosion resistance. The two-phase misfit of the LSP-treated specimen is declined after heat exposure at 850 °C for 2 h, thereby improving the corrosion resistance. However, LSP-treated specimens without heat exposure show CRS as a major factor in improving the corrosion resistance of SC alloy though LSP induces a high two-phase misfit. Therefore, the CRS and two-phase misfit both influence the corrosion resistance of SC alloys. CRS can increase the corrosion resistance, while two-phase misfit deteriorates the corrosion resistance of SC alloys.

### 3 Conclusions

1) LSP introduces a plastic deformation layer in the surface region of SC superalloy containing compressive residual stresses, work hardening, and significantly different dislocation structures in  $\gamma/\gamma'$  phases. The non-uniformly distributed dislocations in  $\gamma/\gamma'$  phases increase the two-phase misfit.

2) The electrochemical corrosion tests of LSP-treated specimens without heat exposure indicate an increase in

corrosion resistance which is attributed to CRS and dislocation defects induced by LSP. The corrosion products consist mainly of Ta<sub>2</sub>O<sub>5</sub> and WO<sub>3</sub> oxides as confirmed by XPS analysis.

3) The electrochemical corrosion tests of LSP-treated specimens after heat exposure confirm that CRS and two-phase misfit are major factors influencing the corrosion resistance of SC alloys. CRS can increase the corrosion resistance while two-phase misfit deteriorates the corrosion resistance of SC alloys.

## References

- Liu L, Meng J, Liu J L et al. *Journal of Materials Science & Technology*[J], 2019, 35: 1917
- Liu Y X, Lei X W, Hao L Y et al. *Applied Surface Science*[J], 2022, 576: 151 785
- Yang Y Q, Wen Z X, Zhao Y C et al. *Corrosion Science*[J], 2020, 170: 108 643
- Lei X W, Nuan V L, Deng Y C et al. *Corrosion Science*[J], 2022, 203: 110 340
- Kovaci H, Bozkurt Y B, Yetim A F et al. *Surface & Coatings Technology*[J], 2019, 360: 78
- Chen T, John H, Xu J et al. *Corrosion Science*[J], 2013, 77: 230
- Luo K Y, Wang C Y, Cui C Y et al. *Journal of Alloys and Compounds*[J], 2019, 782: 1058
- Karthik D, Swaroop S. *Optics & Laser Technology*[J], 2019, 120: 105 727
- Wang H, Ning C Y, Huang Y H et al. *Optics and Lasers in Engineering*[J], 2017, 90: 179
- Karthik D, Stango S A X, Vijayalakshmi et al. *Surface & Coatings Technology*[J], 2017, 311: 46
- Li Y F, Shang X F, Zhai M G et al. *Journal of Alloys and Compounds*[J], 2019, 919: 165 761
- Liu H F, Tan C K I, Cheng W S et al. *Metallurgical and Materials Transactions A*[J], 2020, 51: 3180
- Wang X, Zhang T, Huang Z H et al. *Rare Metal Materials and Engineering*[J], 2018, 47: 1668
- Kubásek J, Molnárová O, Čapek J et al. *Materials Characterization*[J], 2021, 174: 111 037
- Lu G X, Liu J D, Qiao H C et al. *Optics & Laser Technology*[J], 2017, 91: 116
- Geng Y X, Dong X, Wang K D et al. *Optics & Laser Technology*[J], 2020, 123: 105 917
- Tang Z H, Wang K D, Geng Y X et al. *The International Journal of Advanced Manufacturing Technology*[J], 2021, 113: 1973
- Geng Y X, Mo Y, Zheng H Z et al. *Corrosion Science*[J], 2021, 185: 109 419
- Dhakal B, Swaroop S. *Journal of Materials Processing Technology*[J], 2020, 282: 116 640
- Zhang J C, Liu L, Huang T W et al. *Journal of Materials Science & Technology*[J], 2021, 62: 1
- Xia W S, Zhao X B, Yue L et al. *Journal of Materials Science & Technology*[J], 2020, 44: 76
- Long H B, Liu Y N, Kong D L et al. *Journal of Alloys and Compounds*[J], 2017, 724: 287
- Zhang H P, Cai Z Y, Chi J X et al. *Optics & Laser Technology*[J], 2022, 148: 107 726
- Long H B, Mao S C, Liu Y N et al. *Journal of Alloys and Compounds*[J], 2018, 743: 203
- Shen X J, Shukla P, Nath S et al. *Surface & Coatings Technology*[J], 2017, 327: 101
- Wang C X, Jiang C H, Chai Z et al. *Surface & Coatings Technology*[J], 2017, 313: 136
- Milošev I, Žerjav G, Moreno J M C et al. *Electrochimica Acta*[J], 2013, 99: 176
- Yang Y J, Jin Z S, Ma X Z et al. *Journal of Alloys and Compounds*[J], 2018, 750: 757
- Osório W R, Cheung N, Spinelli J E et al. *Journal of Solid State Electrochemistry*[J], 2007, 11: 1421
- Cheng J, Li F, Zhu S Y et al. *Tribology International*[J], 2017, 115: 483
- Lu J W, Zhang Y, Huo W T et al. *Applied Surface Science*[J], 2018, 434: 63
- Huang R, Han Y. *Materials Science and Engineering C*[J], 2013, 33: 2353
- Chen X D, Li Y S, Zhu Y T et al. *Journal of Nuclear Materials*[J], 2019, 517: 234
- Wu X X, Makineni S K, Kontis P et al. *Materialia*[J], 2018, 4: 109
- Carranza R M, Rodríguez M A. *npj Materials Degradation*[J], 2017: 1
- Haynes W M. *CRC Handbook of Chemistry and Physics*[M]. Boca Raton: CRC Press, 2007
- Cwalina K L, Demarest C R, Gerard A Y et al. *Current Opinion in Solid State & Materials Science*[J], 2019, 23: 129
- Sherif E M, Almajid A A, Latif F H et al. *International Journal of Electrochemical Science*[J], 2011, 6: 1085
- Mareci D, Chelariu R, Gordin D M et al. *Acta Biomaterialia*[J], 2009, 5: 3625
- Sure J, Vishnu S M, Kumar R V et al. *Materials Today Communications*[J], 2021, 26: 101 786
- Turdean G L, Craciun A, Popa D et al. *Materials Chemistry and Physics*[J], 2019, 233: 390
- Long X P, Hang T, Guo Y K et al. *Materials Chemistry and Physics*[J], 2020, 239: 121 989
- Wan Z D, Dai W, Guo W et al. *Journal of Manufacturing Processes*[J], 2022, 80: 718
- Lu J Z, Luo K Y, Yang D K et al. *Corrosion Science*[J], 2012, 60: 145
- Ming T Y, Peng Q J, Han Y L et al. *Materials Chemistry and Physics*[J], 2023, 295: 127 122
- Dong Z Q, Liu Z, Li M et al. *Journal of Nuclear Materials*[J], 2015, 457: 266

## 激光冲击强化镍基单晶高温合金的电化学腐蚀行为

耿永祥<sup>1,2</sup>, 郑海忠<sup>1,2</sup>, 李贵发<sup>1,2</sup>, 肖怡新<sup>1,2</sup>

(1. 南昌航空大学 轻合金加工科学与技术国防重点学科实验室, 江西 南昌 330063)

(2. 南昌航空大学 材料科学与工程学院, 江西 南昌 330063)

**摘要:** 采用激光冲击强化技术处理了镍基单晶高温合金, 随后分别热暴露于750和850 °C下2 h, 研究了其在3.5% NaCl溶液中的电化学腐蚀行为。结果表明, 激光冲击强化处理增加了镍基单晶合金的耐蚀性, 这与其诱导的残余压应力和 $\gamma/\gamma'$ 两相中的位错结构有关。 $\gamma/\gamma'$ 两相中非均匀分布的位错增加了两相错配度。热暴露后激光冲击强化试样电化学腐蚀试验表明, 残余压应力和两相错配度是影响单晶合金耐蚀性的2个主要因素。残余压应力可以提高单晶合金的耐蚀性, 而两相错配度则降低了单晶合金的耐蚀性。此外, 单晶合金耐蚀性的提高也与 $Ta_2O_5$ 和 $WO_3$ 氧化物的形成有关。

**关键词:** 镍基单晶高温合金; 激光冲击强化; 电化学腐蚀; 错配度; 残余压应力

作者简介: 耿永祥, 男, 1987年生, 博士, 讲师, 南昌航空大学材料科学与工程学院, 江西 南昌 330063, 电话: 0791-86453203, E-mail: 70959@nchu.edu.cn